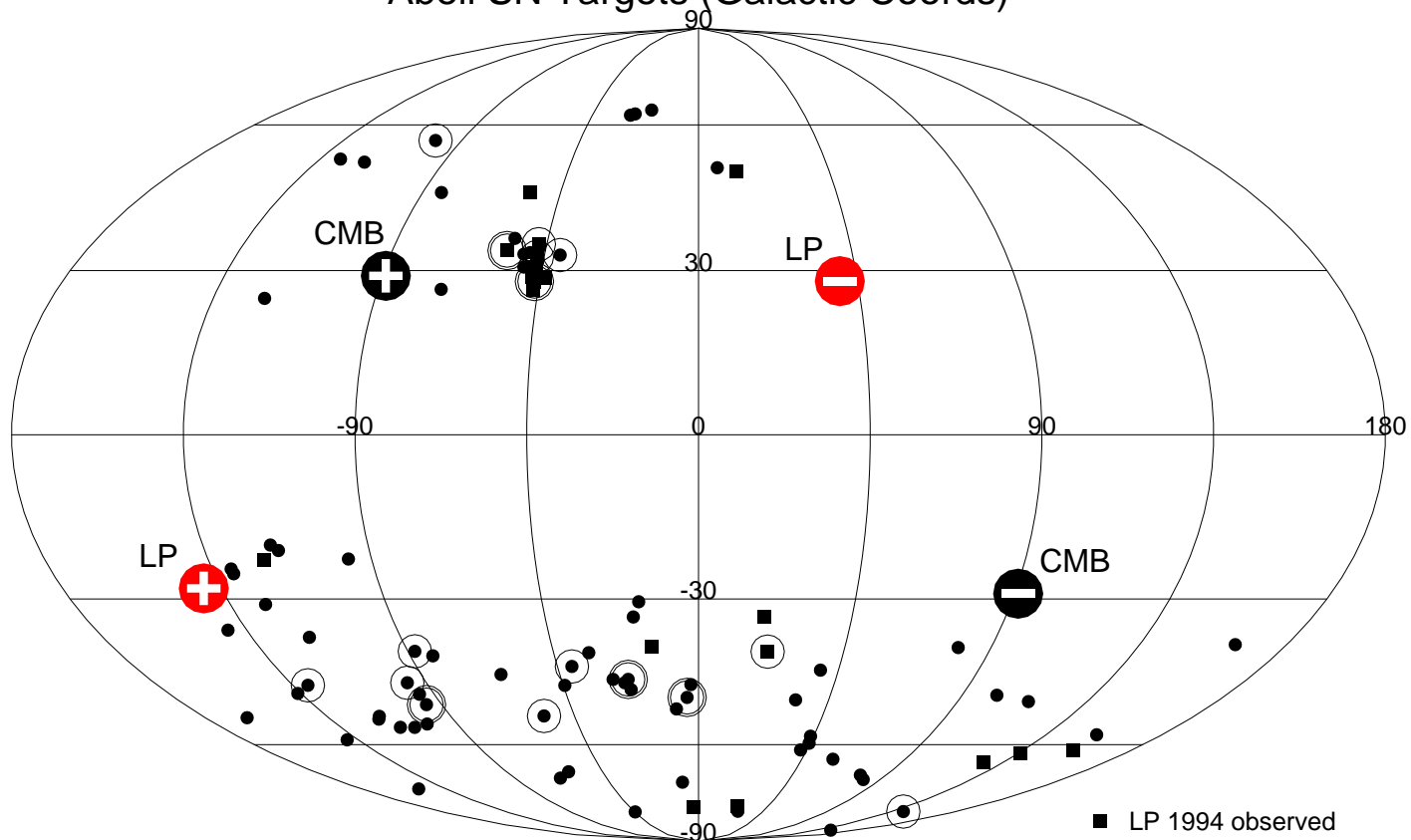
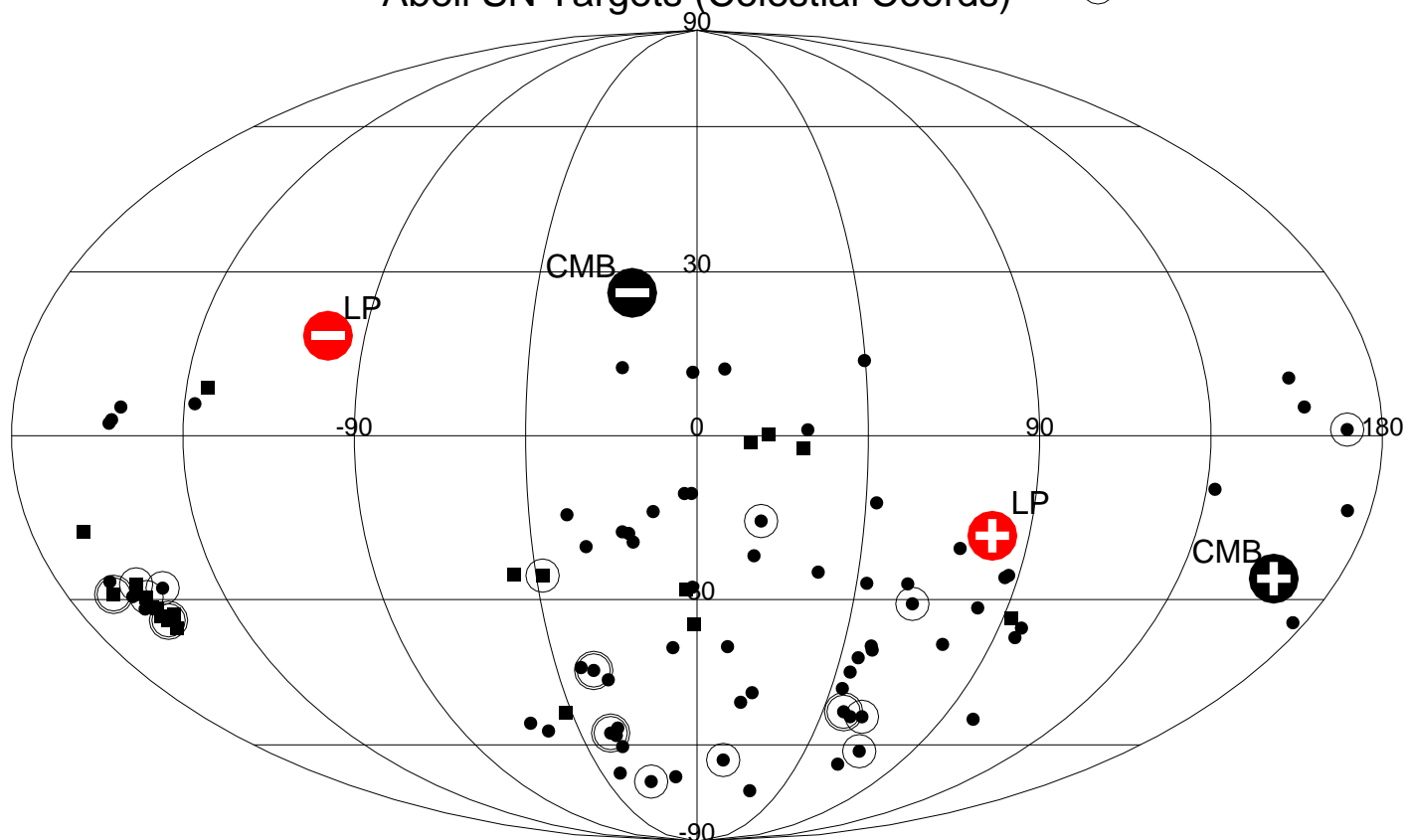


Abell SN Targets (Galactic Coords)



- LP 1994 observed
- LP not observed
- SN detected

Abell SN Targets (Celestial Coords)



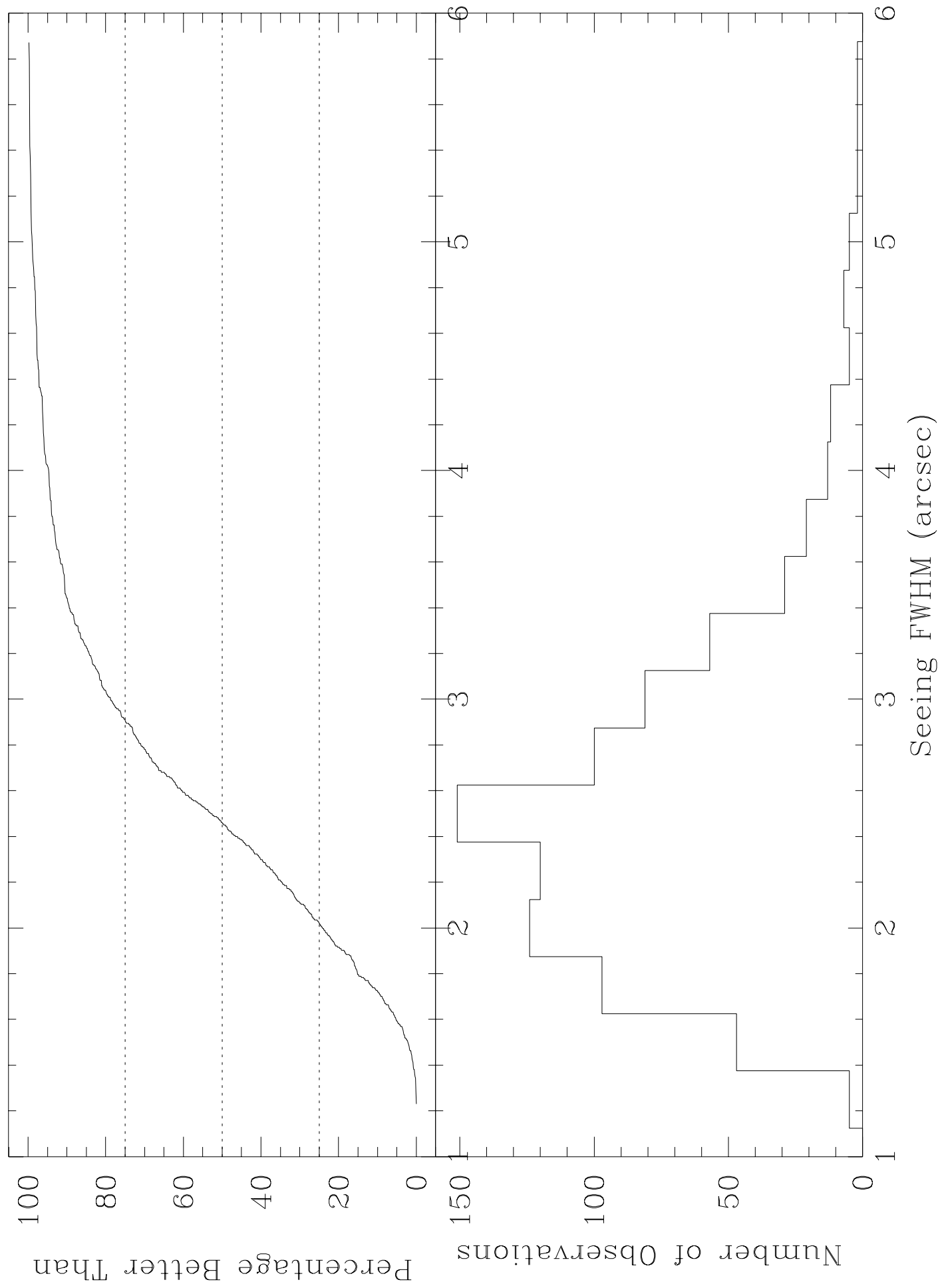


TABLE 2. Supernovae discovered in the Mt. Stromlo Abell Cluster Supernova Search, to date.

SN	Date Found	Not Present	Abell	Type	z	Cluster z
1996af	12 Jun 96	16 May	3879	?	0.10	0.067
1996ag	12 Jun 96	22 May	3809	?	0.14	0.062
1996aj	15 Jun 96	28 May	3559	Ia	0.11	0.046
1996am	12 Jul 96	3 July	3809	Ia	0.065	0.062
1996ao	2 Aug 96	24 June	3128	?	0.060	0.060
1996ap	11 Aug 96	2 Aug	3806	?	0.075	0.076
1996bm	4 Oct 96	1 Sep	2819	?	?	0.075
1996bx	28 Nov 96	23 Aug	3202	Ia	0.06	0.069
1997by	27 Apr 97	4 Apr	1736	Ia	0.045	0.046
1997bz	27 Apr 97	11 Apr	1238	Ia	0.03	0.072
1997cl	2 May 97	5 Aug 96	3577	II-n	0.047	0.050
1997cm	2 May 97	15 Mar	3528	?	0.07	0.053
1997cp	2 Jun 97	11 May	3806	?	0.16	0.076
1997cr	2 Jun 97	17 Aug 96	3744	II	0.077	0.038
1997cu	4 Jul 97	25 Feb	3128	Ia	0.062	0.060
1997cv	7 Jul 97	10 June	3565	?	?	0.012
1997??	10 Jul 97	16 June	151	?	?	0.053
1997cz	19 Jul 97	26 Apr	3565	?	?	0.012
1997cy	16 Jul 97	12 Mar	3266	?	?	0.059

Notes to Table 2.

The ‘Not Present’ column lists the most recent date of observation prior to discovery in which the SN was not visible. Unnamed SNe have not been published in an IAU Circular.

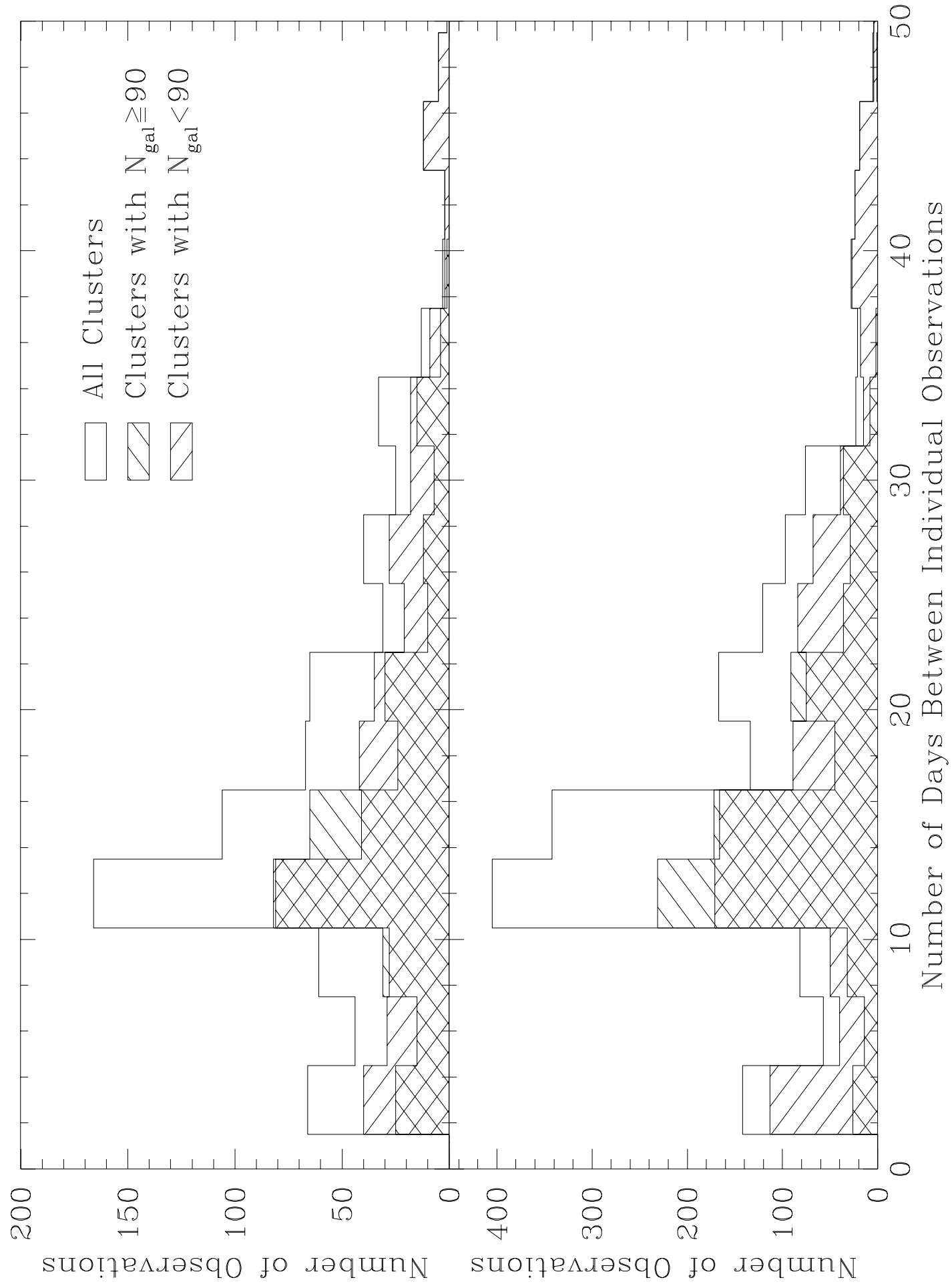


TABLE 3. Expected uncertainties in the measurement of the three components of the reflex motion of the Local Group in a sample of SNe Ia of size N_{SN} .

N_{SN}	km s ⁻¹		
	σ_x	σ_y	σ_z
20	545	545	300
40	325	325	185
60	245	250	140

This figure "snsearch.fig4a.jpg" is available in "jpg" format from:

<http://arXiv.org/ps/astro-ph/9710037v2>

This figure "snsearch.fig4b.jpg" is available in "jpg" format from:

<http://arXiv.org/ps/astro-ph/9710037v2>

This figure "snsearch.fig4c.jpg" is available in "jpg" format from:

<http://arXiv.org/ps/astro-ph/9710037v2>

This figure "snsearch.fig4d.jpg" is available in "jpg" format from:

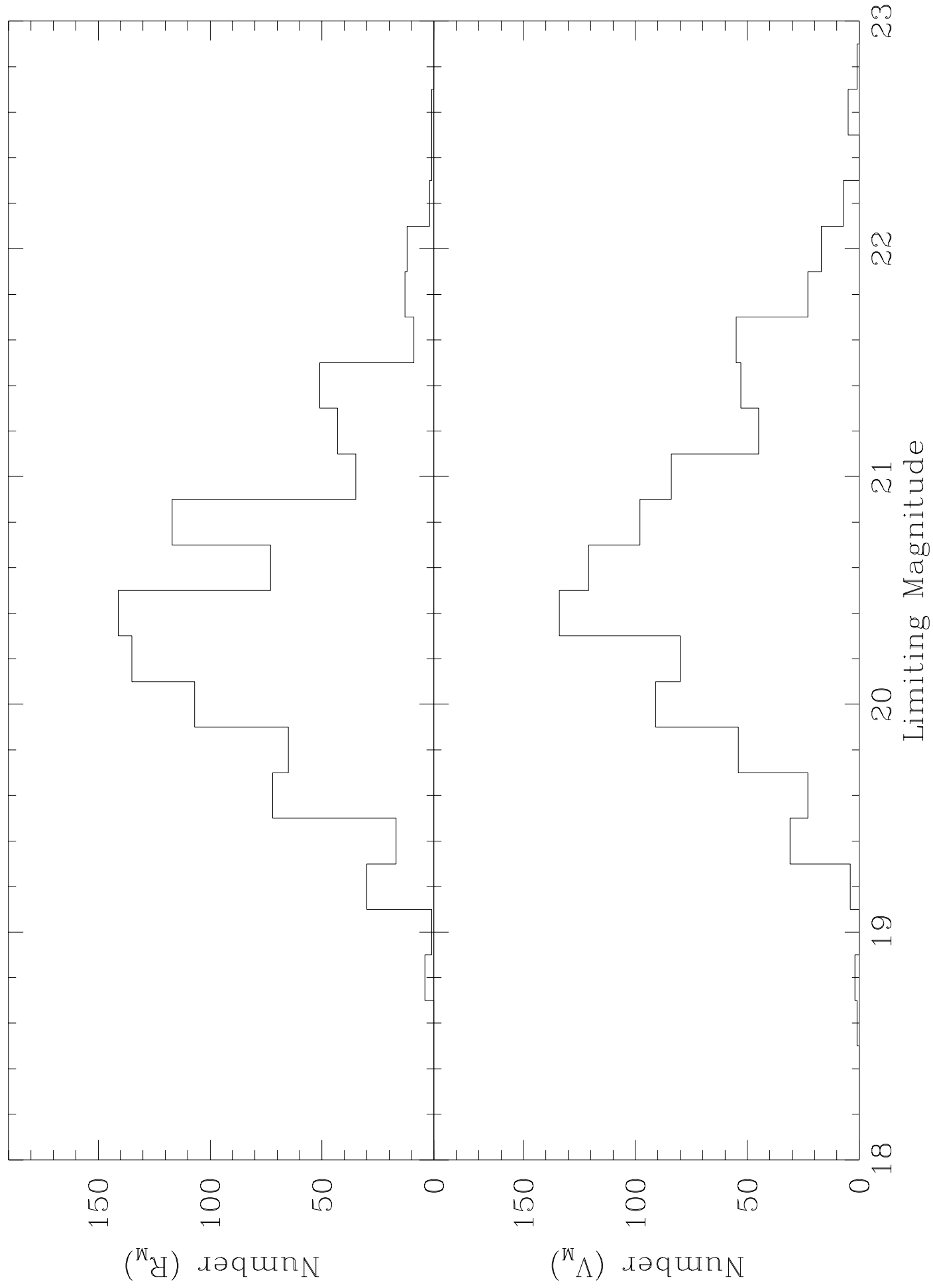
<http://arXiv.org/ps/astro-ph/9710037v2>

This figure "snsearch.fig4e.jpg" is available in "jpg" format from:

<http://arXiv.org/ps/astro-ph/9710037v2>

This figure "snsearch.fig5.jpg" is available in "jpg" format from:

<http://arXiv.org/ps/astro-ph/9710037v2>



The Mount Stromlo Abell Cluster Supernova Search

David J. Reiss

Dept. of Astronomy, University of Washington

email: reiss@astro.washington.edu

Lisa M. Germany

Mount Stromlo and Siding Spring Observatories

email: lisa@mso.anu.edu.au

Brian P. Schmidt

Mount Stromlo and Siding Spring Observatories

email: brian@mso.anu.edu.au

and

C. W. Stubbs

Depts. of Physics and Astronomy, University of Washington,

Mount Stromlo and Siding Spring Observatories

email: stubbs@astro.washington.edu

http://msowww.anu.edu.au/~reiss/Abell_SNSearch

Subject headings: surveys, methods: observational, techniques: image processing, supernovae: general, distance scale

ABSTRACT

We have initiated a three-year project to find supernovae (SNe) in a well-defined sample of high-density southern Abell clusters with redshifts $z \leq 0.08$. These observations will provide a volume-limited sample of SNe Ia to more than a magnitude below their peak brightness, and will enable us to: (1) measure the luminosity function of SNe, (2) further explore the correlation of light curve shape with the absolute luminosity of SNe Ia to better understand SNe Ia as distance indicators, (3) measure SN rates, (4) measure the bulk motion of the Local Group using SNe Ia, and (5) directly compare SN Ia distances to brightest cluster galaxy distances. We use the MaCHO wide-field 2-color imager on the 1.3m telescope at Mount Stromlo to routinely monitor ~ 12 clusters per week. We describe our technique for target selection and scheduling search observations, and for finding and identifying SN candidates. We also describe the results from the first year of our program, including the detection of 19 SNe, several RR-Lyrae variables, and hundreds of asteroids.

1. Introduction and Motivation

As extremely luminous point sources which represent a discrete physical event, SNe are attractive indicators of extragalactic distances. The CTIO/Calán group (Hamuy *et al.* 1995; Hamuy *et al.* 1996a) demonstrated that Type Ia SNe are not standard candles but instead show a range in peak luminosity of approximately one magnitude in V . However, they also proved that there exists a tight correlation between decline rate and peak brightness for SNe Ia in the sense that more luminous events decline more slowly than intrinsically faint ones (Phillips 1993). This property of SN Ia light curves provides a means to accurately estimate the intrinsic luminosity of the SN, thereby sharpening the precision of SNe Ia as standard candles to better than $\sigma_V < 0.2^m$. A somewhat more elaborate method developed by Riess, Press, & Kirshner 1995a, 1996 uses multi-band light curve shapes to estimate the luminosity of type Ia SNe and also predicts distance uncertainties and extinction for individual SNe. Using a sample of 20 SNe drawn from Hamuy *et al.* 1996b and their own observations, they were able to improve the distance estimate for each, decreasing the scatter in the Hubble diagram to $\sigma = 0.12^m$ (distance error of 6%).

For type Ia SNe to be useful for measuring distances, they must be discovered near peak brightness. Searches based on infrequent observations typically produce SNe that are too old to obtain good followup photometry and measure well-sampled light curves. In a systematic search in which each field is revisited periodically, the ages of any discovered SNe are constrained to be less than the time since the field was last observed. Such frequent visits enable more accurate light-curve shape measurements, and thus, more accurate distances. Systematic searches for distant SNe ($z \gtrsim 0.4$) are currently being carried out by Perlmutter *et al.* 1997 and Schmidt *et al.* 1997b while nearby searches are being conducted by groups at the Beijing Astronomical Observatory (d. Li *et al.* 1997), the Perth Observatory (Martin, Williams, & Woodings 1997), U.C. Berkeley (Treffers *et al.* 1997), and by R. Evans (Evans 1997). These searches fill in the distant and nearby ends of the Hubble diagram, respectively. Though many SNe have been found at $0.002 < z < 0.2$, selection effects plague most samples, and are nearly impossible to quantify. A well-understood, complete sample of SNe in this intermediate distance range is needed so that we can understand the uncertainties and biases which arise from calibrating the distant samples using the nearby objects. The search described in this paper is optimized for finding SNe over the range of redshifts $0.02 \leq z \leq 0.08$ with a completeness limit fainter than $V > 20$. Complimentary searches scanning lower-redshift Abell clusters (Maza *et al.* 1997) and Northern hemisphere Abell clusters (Adams *et al.* 1997) have also been initiated. The SNe produced by these searches, when combined with objects from the nearby and distant searches, will comprise a sample of SNe encompassing a broad range of distances with which we can accurately map out the expansion of the Universe from $0.002 \leq z \leq 1.0$.

To understand the systematics involved in using SNe as distance indicators, we need to understand the SNe, their evolution, and their progenitors better. Supernova rates, for example, place important constraints on models of progenitor evolution and the physical processes involved in the explosions, in addition to star formation and chemical enrichment. However, they are still subject to dispute, particularly due to interpretations of selection effects and control times and the large statistical uncertainties of small samples (see Cappellaro *et al.* 1993, Tammann 1994). Our sample will be unique in that it is volume-limited to more than a magnitude below the SN Ia average brightness for our most distant clusters, and its selection criteria are well understood. These properties will allow us to estimate and compare rates of SNe of different types, both in the clusters, and in the field surrounding them.

Knowledge of the luminosity distribution of SNe Ia would enable us to place constraints on the systematics (such as Malmquist bias) introduced by using SNe Ia as distance indicators. However, the SN Ia luminosity function is largely unknown due to poor understanding of the selection effects of past searches. An important aspect of this is the evolution of the luminosities of SNe Ia. Hamuy *et al.* 1996a have shown that there appears to be an intrinsic difference in the peak luminosity–decline-rate relationship between the nearby Phillips 1993 sample and their more distant sample of SNe Ia. In addition, there appears to be a strong correlation between the decline rate of SNe Ia and the host galaxy type; SNe Ia that occur in early-type galaxies have preferentially narrower light curves than those in their spiral counterparts. Fortunately, after correcting for light curve shape, there is no detectable differences between distances measured to early- and late-type galaxies (Schmidt *et al.* 1997a). Our SN sample should allow us to construct a SN Ia luminosity function and to explore the effects of the host galaxy type, progenitor stellar population ages, and environment (cluster vs. field) on SN luminosities. This will enable us to place limits on these evolutionary effects and to estimate any biases which they might introduce into estimates of q_0 via SNe Ia.

The intermediate-distance SNe are also ideally suited for measuring the reflex motion of the Local Group (LG), unhindered by random peculiar velocities of nearby galaxies or large uncertainties in measuring distances of very distant objects. Lauer and Postman (1994) [LP94] determined distances to Abell clusters within $z < 0.05$ using brightest cluster galaxies (BCG) as distance indicators with an accuracy of 16%. Their controversial result suggested that these clusters participate in a large bulk motion (560 km sec^{-1}) pointing nearly 70° away from the direction of the dipole in the microwave background (CMB) as measured by COBE (Fixsen *et al.* 1994). The amplitude of their measurement within such a large volume contradicts many currently popular models (Feldman & Watkins 1994, Strauss *et al.* 1995). While other studies of Abell clusters (Hudson & Ebeling 1997, Branchini,

Plionis, & Sciama 1996) have questioned the significance of the LP result, other reanalyses (Colless 1995, Graham 1996) have supported their claims, and simulations have confirmed the notion that dense clusters can readily be used to trace the large-scale structure of the universe (Gramann *et al.* 1995).

Studies of large-scale motions using other distance estimators have since been attempted to test the validity of the LP result. In particular, Riess, Press, & Kirshner 1995b [RPK95] used a sample of 13 SNe Ia to measure peculiar velocities to galaxies in the field. Using the uncertainties in the SN Ia distance measurements which are computed directly from their multi-color light-curve shapes technique, they found that they can rule out the LP measurement at a confidence level better than 99.3%. Moreover, their velocity estimate is consistent with a bulk motion of similar amplitude and direction to the velocity dipole in the CMB. Still other peculiar velocity samples constructed using different distance indicators, such as Tully-Fisher measurements (Giovanelli *et al.* 1996), also seem to disagree with LP94. However, Watkins & Feldman 1995 argued that in contrast to the BCG sample of LP94, these more recent measurements are sensitive to small-scale motions, to different degrees (since motions of rich galaxy clusters are less sensitive to small-scale flows) and this significant source of noise reduces their overall sensitivity to the large-scale motions. Therefore, because these samples probe different locations in space where the small-scale flows differ, this results in decreasing, but not eliminating, the significance of the disagreement between the bulk motion measurements of LP94 and RPK95 (and by extension the Tully-Fisher measurements of Giovanelli *et al.* 1996).

The Abell cluster targets in this search are a subset of the clusters currently being observed as part of a larger BCG survey by Postman, Lauer and Strauss (PLS). The resulting sample of cluster peculiar velocities from SNe Ia will be directly comparable to the BCG measurements which will emerge from the LP94 + PLS surveys, allowing a direct comparison of SN Ia distances and BCG distances to many clusters. This will enable us to measure the reflex motion of the LG with respect to a subset of the LP94 + PLS clusters using an independent distance indicator which offers significantly increased precision, and which can be directly compared to that of LP94 and/or PLS, in contrast to the other surveys mentioned above. The contribution that this SN search can make to the bulk motion question is examined in detail in Section 6. Finally, the large-scale velocity field of Abell clusters derived from our sample of SNe can be compared to those predicted by the gravity fields of all-sky galaxy catalogs and simulations, to test models of structure formation and constrain $\Omega_0^{0.6}/b$, where b is the biasing parameter, similar to the analysis performed on a sample of 25 SNe Ia in the field by Riess *et al.* 1997.

Additional projects of interest which may emerge from this project include: (1) placing

limits of low-mass intracluster MaCHOs ($\sim 10^{-4}M_{\odot}$) by trying to detect microlensing light curves on top of the light curves of SNe which are found on the far side of their cluster fields (Kolatt & Bartelmann 1997), (2) detecting the tidal disruption and accretion of stars into the central black holes of AGN through flares in the AGN luminosity (Evans & Kochanek 1989), and (3) detecting RR-Lyrae in the halo of our galaxy, useful for tracing its kinematics.

2. Search Strategy

The difficulty in searching for intermediate-distance supernovae is that one cannot practically target individual galaxies with short exposure times as in nearby searches, while the volumes (and galaxy numbers) being sampled are much smaller than those in the high-redshift searches. One must survey a large area of sky at locations where the galaxy number density is the largest at the desired distance, using an intermediate-sized telescope. The Mount Stromlo Abell Cluster Supernova Search employs the MaCHO wide-field ($45' \times 45'$) dual-color mosaic imager (Stubbs *et al.* 1993) on the MSSSO 1.3m telescope (Hart *et al.* 1996). The camera’s passbands are not standard and we refer to them as V_M for the ‘blue’ side and R_M for the red side. We specifically target all high-density ($N_{gal} \equiv$ number of galaxies within one Abell radius ≥ 65) clusters from the Abell, Colwin and Owen (ACO, 1989) survey of nearby, rich galaxy clusters. The target clusters are further constrained to lie within $z \leq 0.08$ as measured in the BCG survey of PLS, and to be accessible at reasonable altitude from Stromlo ($\delta(J2000) \leq +15$). The complete sample of 74 clusters is listed in Table 1; their distribution in the sky is displayed in Figure 7. In all there are 20 clusters in our sample whose BCG distances were measured by LP94. Note that the sample’s large-scale distribution on the sky is not uniform; in particular nearly 1/6 of the target clusters are located in the direction of the Shapely-Ames Supercluster near $(l, b) \sim (315, +30)$.

Our project has been allocated 5% of the telescope time on the 1.3m, the remaining 95% belonging to the MaCHO project, with all of our images being observed by the MaCHO staff observer. A typical SN Ia at $z = 0.08$ has $M_B \sim 18.5$ near maximum light. Type II and Ib/c SNe are 0 to 5 magnitudes fainter. In order to be complete in detecting point sources at 20th magnitude, the faintest objects which we can readily follow up with photometry and spectroscopy, with $2.5''$ FWHM seeing that is typical at MSO (Figure 7 shows the distribution of observed FWHM over the past year), we take 240-second exposures of each field. Therefore we have enough time to average ~ 4 to 5 observations night $^{-1}$. The

telescope time is most efficiently used (with less overhead) by observing ~ 14 fields every third night. Allowing for weather ($\sim 50\%$), we average ~ 14 fields per week, enough to observe $\sim 1/3$ of the 74 fields in the two-week period that it takes for a SN Ia to reach peak brightness.

The Macho camera’s pixel scale of $0.628''/\text{pixel}$, combined with the $\sim 2.5''$ typical FWHM, allows for good sampling of the PSF, which is important in the image subtraction process used to detect SNe, as described in §4. The dual mosaic focal plane is read out at 16 separate amplifiers, resulting in 15 separate 1024×2048 -pixel images (8 in blue and 7 in red because of one dead amplifier) which sample the entire $45'$ field. This also is advantageous for the subtraction process, as will be explained below.

High-quality and frequent followup photometric and spectroscopic observations are extremely important for the success of this project. In addition to the images from the 1.3m,¹ we obtain regularly scheduled observations on the MSSSO 2.3m (spectra and imaging), and the MSSSO 1.9m. The ARC 3.5m is also employed for spectroscopic followup on SNe detected at $\delta \gtrsim -30$. In addition, we use a semi-dedicated (shared with the MaCHO group) $30''$ at MSSSO as our main source of photometric coverage. The nightly observations are conducted by the RAPT group of amateur astronomers and observers, who are an invaluable asset to this program.²

3. Scheduling and Data Collection

An automated scheduling routine is used to determine which fields (of those that satisfy the criteria described in §2) are best for observing on a given night, and at what time. The algorithm is summarized below:

1. A field is ineligible for observing on any given night if:
 - (a) its hour angle at evening twilight is $\text{HA}_{eve} > 2$ hours, or
 - (b) its hour angle at morning twilight is $\text{HA}_{morn} < -4$ hours. This ensures that the clusters will be observable for at least 6 weeks (allowing sufficient followup).

¹The non-standard V_M and R_M passbands can be accurately transformed to rest-frame B and R_C (0.01 mag r.m.s.) as described by Kim, Goobar, & Perlmutter 1996, because they are well matched to these filters redshifted to $z \sim 0.06$ (Germany *et al.* 1997).

²For more information on the RAPT group, please see <http://www.tip.net.au/~bnc/>.

2. Assign a weight w_i (which is a function of time, t) to each of the remaining fields, i :

$$w_i(t) = \left(\frac{N_{days,i}}{21} \right)^2 \times \frac{N_{gal,i}}{100} \times \frac{X_i(t)}{X_{min,i}}, \quad (1)$$

where $N_{days,i}$ is the number of days since the i^{th} field's last observation, $N_{gal,i}$ is its ACO galaxy count, $X_i(t)$ is its current airmass, and $X_{min,i}$ is the minimum airmass which it reaches at Mount Stromlo.

- (a) Special consideration is taken for fields which are being observed for the first time this season so that they don't dominate the schedule.
 - (b) If the night is dark and the seeing good (better than $2''$), weights for fields which have not yet been observed are artificially inflated to allow more template observations on good nights (see §4.1).
 - (c) Weights for fields which have been observed within the past week are artificially reduced so they cannot be observed at the expense of other fields.
 - (d) Individual clusters can be given higher priority, as desired, for example, to increase the frequency of observations made of clusters with current SNe, or those with possible SNe which need confirmation.
3. The time, t_c , which maximizes the sum of weights of all observable fields, $\sum_i w_i(t)$, is chosen as the best time to observe.
 4. Queue the fields which are observable at time t_c by their weight $w_i(t_c)$, filling up the allocated 15% of the night (including time for CCD readout and telescope slewing).³
 - (a) Skip those clusters which lie less than 20° from the moon.
 - (b) Also skip those clusters which lie at $X_i(t_c) > 2.0$.
 5. Sort the scheduled fields by their azimuthal angle to provide the telescope with the shortest slewing path between observations.

The routine creates a 'scheduler file' which lists the coordinates of the scheduled fields; this is fed directly into the MaCHO camera/telescope controller system at the requested time, t_c . The automated system takes over at that point until all exposures are finished. The resulting bias-subtracted, flat-fielded images are then copied to local disk for analysis.

³Though steps 4a and 4b logically should come prior to step 3, our scheduling follows this sequence so that we do not use more than our 5% share of dark time on the 1.3m. There are usually sufficient numbers of clusters needing observations that this procedure does not result in any wasted observing time.

The amount by which each factor in Eq. 1 contributes to the cluster weights has been tuned so that on average, each cluster is revisited every fortnight – even those with the lowest galaxy counts in our sample. This system has worked extremely well; to date $\sim 4.7\%$ of the usable telescope time has been used to observe Abell clusters. As shown in Figure 7 (top), for the observations of the past year, the median time-between-observation (Δt) of each field is 12 to 15 days, with a strongly peaked distribution (this histogram also includes the observations taken during the first few months of the search, in which the scheduler was being ‘tuned’). A very similar distribution is obtained from a simulation of 3 years’ observations in which a random 50% of the nights are skipped (Fig. 7, bottom). It is evident from Fig. 7 that a number of clusters do not get observed for 3 weeks or more, but this is to be expected when random weather patterns, the moon, scheduled followup, and candidate object re-observations, etc. are considered. We have recently introduced other measures which we expect will decrease the large number (though still $< 10\%$) of observations for which $\Delta t = 3$ days. Still, 80% of the observations were made with $\Delta t \leq 21$ days, and although sparser clusters do slip through the cracks more easily, as Fig. 7 demonstrates, the amount of favor given to larger clusters is small. The overall results are more than adequate, and we believe the scheduling could not be substantially improved by a human counterpart.

4. Searching for Supernovae

The software which searches the images for supernovae consists of a series of IRAF tasks and programs written in C, linked together and automated via a set of scripts written in PERL, with final cuts on potential discoveries being made interactively. Briefly, it involves subtracting an earlier observation of the field (a *template*) from the observation so that all objects which have increased in flux appear as new point-sources. No attempt is made to combine the 8 amplifier images for each color into one 4096×4096 image prior to searching; instead each amplifier is processed individually. This has several advantages and one disadvantage, which will be pointed out below. Figure 7 illustrates the method, which can be summarized by the following expression:

$$\mathcal{S} = b \times (a + \mathcal{O} * \mathcal{K}) - \mathcal{T}, \quad (2)$$

where the subtracted image, \mathcal{S} , is scanned for new objects. Here, \mathcal{T} is the template of the field, \mathcal{O} is the observation (registered to the template), \mathcal{K} is a convolution kernel required to match the PSF of \mathcal{O} with that of \mathcal{T} , and a and b are an additive constant and linear scale factor, respectively, which match the background and flux of objects in \mathcal{O} to those in \mathcal{T} . The following sections describe the algorithm in detail.

4.1. Constructing the Template

Before any image subtraction can be done, a template of the field must be constructed. This involves (1) preprocessing – masking of saturated stars and bright pixels and removing any linear gradients in sky brightness (all observations are pre-processed identically); (2) detecting bright stars for image alignment (we use DoPhot, Schechter, Mateo, & Saha 1993, which also provides an analytic model of the stellar PSF); (3) identifying isolated high S/N stars of differing brightness for use in PSF and flux matching, and (4) laying down a grid of (negative) false stars of known flux for quick assessment of searching depth after the template is subtracted from the observation. The template is made using an observation obtained preferably during a dark, transparent night with good seeing. If a later observation proves to be better than the template, the template is replaced after that observation has been searched. This is a simple procedure since the process is completely automated. A section of an example template is shown in Figure 7a.

4.2. Image Registration

The most important aspect of the image subtraction process is accurately aligning the observation images to the template images. The registration is accomplished using a triangle-matching algorithm (see Groth 1986) to determine the coordinate transform between bright stars found using DoPhot in the two images. In our case since the template and observations are always taken on the same telescope/camera system, we can constrain the rotation and scale in the transform, which allows a more robust convergence with fewer failures. The transform is then entered into the IRAF GEOTRAN routine which performs the flux-conserving linear geometric transform of the observation image, using a linear interpolation between pixels for subsampling. Since the PSF is well sampled, resampling errors are small. The registration typically requires a shift of < 50 pixels and is accurate to ~ 0.3 pixels across an entire individual amplifier image. This process is aided by not registering the entire $45'$ field at once; the effects of variations in pixel scale across the field are reduced and higher-order transformations rendered unnecessary. However, it does result in a loss of ~ 50 pixels of searchable area near the edges of each amplifier image after the registration. In Figure 7b we present a portion of an observation before (left) and after (right) it is registered with the template of Figure 7a.

4.3. PSF Matching

If the observation and template were both photometric and their PSFs were identical, a simple subtraction would now be suitable. Unfortunately, this is almost never the case. Instead, we must match the images' PSFs and intensities. For the sake of simplicity, we will assume that we are convolving the template, since the template is usually the better image, and the better of the two images is the one which must be degraded to match the poorer one. The convolution kernel which can be used to convolve the template so that its PSF matches that of the registered observation is computed using Andrew Phillips' implementation of the algorithm of Ciardullo, Tamblyn, & Phillips 1990 (see Phillips & Davis 1995) in IRAF (called QPSF, in the ALINEAR package). Briefly, the method computes the kernel in Fourier space, where a convolution is a simple multiplication. Since the PSF is very nearly Gaussian, its Fourier Transform (FT), and thus the convolution kernel, will also be very nearly Gaussian. However the high-frequency components of the FT become dominated by noise in the wings of the PSF where the signal becomes weakest. Still, one can model the high S/N components of the FT with an elliptical Gaussian, and the wings of such a model can be used in place of the noise-dominated components. Thus a single, bright, isolated star can be used to compute the required convolution kernel. In the case where the two images are similar (FWHMs differ by < 0.3 pixels), the convolution kernel may be very poorly resolved, or even undefined (as might be the case if the PSFs are elongated). One can overcome this problem by degrading the slightly poorer image using a Gaussian convolution kernel before performing the PSF matching. The Fourier method is applied to each of the individual amplifier images, sufficiently reducing the effects of any small-scale PSF variation across the focal plane. The template of Figure 7a is shown in Figure 7d after it has been convolved to match the registered image of Figure 7c.

4.4. Photometric Scaling and Subtraction

For the photometric scaling, as in the PSF matching, all that is required is a high S/N, isolated star or galaxy. The IRAF ALINEAR task, ITRAN (Phillips & Davis 1995), performs a linear least- χ^2 fit to the difference, in ADU, between the pixels which surround the chosen bright object in a subsection of the two images (registered observation and convolved template). The resulting slope (measuring the ratio in flux between the two images) and offset (measuring the difference in sky brightness) can then be applied to the registered observation. The slope, offset, and χ^2 give us further information on the quality of the observation and subsequent subtraction. For example, the star chosen for PSF-matching might be saturated in the observation, say, if the seeing was extremely good,

and the χ^2 will be extremely high. In this case we can go back and match the PSFs and fluxes using a slightly fainter star and check the results. Again it is worth noting that having the focal plane divided into eight smaller images makes the scaling more accurate as any large-scale nonlinear gradients in sky brightness or scattered light (such as due to the moon) or even variation in transparency across the 45' field (due to thin clouds) are reduced. It makes even more sense when one considers that the individual images come from different CCDs and thus have different gains, bias levels, and color terms.

Finally, the intensity-transformed, convolved template now reflects the same atmospheric and photometric conditions as the registered observation, and a simple subtraction of the first from the second can be performed. The subtraction of the convolved template image (Figure 7d), after being photometrically scaled, from the registered observation (Figure 7c) is presented in Figure 7e. Here, a supernova is clearly visible where in the original observation (Figure 7b), it was hidden in the background light of its host galaxy. Five of the (now positive) sensitivity stars are also visible in the subtracted image. The corresponding magnitude limit for this image is $R_M \sim 20.5$ (typical); the supernova is ~ 0.9 magnitudes brighter. Note that the noise in the subtracted image is now a function of Poisson noise (from the shifted observation) plus correlated Poisson noise (from the convolved template) plus residual noise left over from the subtraction.

4.5. Object Detection

Once the subtraction is complete, a new supernova will appear as a point source in the subtracted image, with a FWHM which is the same size as other stars in the original observation. To find these, we use a point-source detection algorithm, written in C, which samples the subtracted image at many locations over the scale of the PSF to estimate the total noise (σ) within one correlation length. It then detects objects with a total flux that is 3σ above the background. If a detection lies at the same location as a bright star on the template, it is assumed to be a poor subtraction, and is eliminated from the list. (Poor subtractions near bright stars are common because the large flux gradients magnify the effects of even a small registration or PSF-matching error; such a residual can be seen above and to the left of the supernova in Fig. 7e.) In addition, our routine tests if each detected object is consistent with a point source of given peak intensity and known FWHM. This helps eliminate cosmic rays, which resemble stars (since they have been convolved) but are slightly narrower than true stars in the image. Often a poor subtraction results in an area of negative flux next to a detected object. Our algorithm tests for these as well and eliminates any such suspicious objects. The routine then eliminates groups of objects

which fall in straight lines (satellite trails or bad columns). As a check on the depth and robustness of the search, the false sensitivity stars which have been detected are identified, and the corresponding limiting magnitude is computed from the known flux of the faintest star detected.

Though the object-detection algorithm has been custom designed to reduce the number of false detections, several hundred usually pass the cuts for each observation. Most of these offenders are cosmic rays; thus, our ultimate defense is that we have two observations made simultaneously, one in V_M and one in R_M . As a final check, the locations and fluxes of the objects detected in the V_M images are compared to those in the R_M images. This serves to cull nearly all cosmic ray hits. In the end, our detections are $\sim 4.5 \sigma$ above the correlated noise (recall this is *not* the Poisson noise of the original image, but can be similar to it in a good subtraction, or significantly greater than it in a poor subtraction). On average 5–15 objects per observation remain, and these comprise poor subtractions near bright galaxies and stars (somewhat common, particularly in poor seeing); cosmic rays which coincidentally lie at the same locations in both color images (rare); and true astronomical objects ($> 95\%$ of which are asteroids). For each of these objects, a subraster image is created, and final cuts are made by eye.

4.6. Subrasters and Object Classification

The layout of a subraster image produced by the search software is shown in Figure 7, in this case, containing the SN seen in Figure 7e. The subrasters allow for quick examination, by including the candidate object in both colors (V_M on the left, R_M on the right), in the template (bottom), observation (top) and subtraction (center). They are archived on disk for quick retrieval and can be accessed at any time by running a script which displays the subrasters, and allows interesting objects to be scrutinized in detail using IMEXAM in a local XIMTOOL window. Alternatively, they can be viewed over the World Wide Web on an interactive web page which displays and then IMEXAMs them in a local XIMTOOL window, and allows object classifications to be recorded in a database for comparison to future observations (see below). Both methods also display the object’s coordinates and approximate magnitudes in both colors. In addition, information on the quality of the observation, such as the scale and offset used in flux-matching, the FWHM, and the number of sensitivity stars detected, are all reported to the classifier. All of these data are used to quickly classify objects among poor subtractions and cosmic rays, asteroids, variable stars which have increased in brightness, and supernova candidates. We find that the human eye is extremely efficient at classifying the objects. A great deal of experience is gained by

examining subrasters day after day, and a certain amount of intuition certainly plays a role in object classification; however certain concrete rules also apply.

SNe, variable stars, and asteroids each have characteristics which aid in their identification, and the color information which we have is extremely helpful. Young supernovae are bluish objects ($V_M - R_M < 0.2$), and are usually associated with a galaxy. If an object lies directly on the nucleus of the galaxy, it is treated with suspicion and is often a poor subtraction or AGN; however we have detected several SNe very near the centers of their host galaxies, SN 1997bz being one example. Asteroids, on the other hand, are usually redder than the color of the Sun ($V_M - R_M > 0.3$), are usually not associated with a galaxy, and upon close inspection often exhibit slightly elongated PSFs (particularly the bright ones). Unfortunately there is a large dispersion (~ 0.5 magnitudes) in the rough uncalibrated $V_M - R_M$ colors computed by the software, thus color discrimination provides an aid but not an end in object classification. Variable stars are straightforward to identify as they are present as a star on the template image, as well as in the observation.

The classification-by-eye scheme is certainly not fail-proof (it is possible that we do misidentify some SNe as asteroids). We overcome this weakness by keeping records of the positions of all objects which we identify. If an object is identified as an asteroid, we can compare its location to those of other objects identified in a later observation of the same field. If it is present at the same location in both observations, it is likely to be a SN rather than an asteroid. On the other hand, any field with a probable supernova as identified by eye is re-observed as soon as possible to see if the object has moved or disappeared; if it has, it is most likely an asteroid. We perform such followup on all objects located near galaxies, regardless of color, and on blue objects not associated with galaxies. In the end, this conservative approach eliminates all possibility of misidentifying an asteroid as a supernova. Our probability of misidentifying a supernova as an asteroid is not zero, but if we re-observe the field within the next few weeks, we are able to correct such misidentifications. However we will still have a diminished sensitivity to SNe with undetected hosts.

5. Results

Once a promising supernova candidate is found, and has also been confirmed with a second observation, it is announced in an IAU Circular. A finder chart with positions accurate to better than $0.5''$ is immediately created using an automated routine, and all available information is placed on our web page. Information on the 19 supernovae discovered by this search to date are listed in Table 2 (we came on line in early June, 1996). Although spectroscopic followup was sparse at the beginning due to weather and technical

difficulties, we anticipate being able to get a redshift and spectral type for nearly all future supernovae. The rate of discovery is about 1.5 month^{-1} . Of the 15 SNe for which redshifts have been measured, 8 appear to be associated with their host Abell cluster, while six lie behind their target clusters, and one is in a foreground galaxy. Six of the nine SNe which have been spectrally classified are SNe Ia. Many of the other SNe have occurred in elliptical galaxies and can be identified as type Ia on that basis alone. We can also, with reasonable reliability, classify SNe using their multicolor light curves. In total, we find that 12 objects, of the 17 which have spectra and/or reduced light curves so far, are SNe \sim Ia, and 7 of these are associated with their host Abell clusters. Two classified SNe are type II and are associated with their host clusters, while one other, classified as type II, is not. The two remaining objects are probably not type Ia, and/or they are not associated with their host clusters. Light curves, classification, and analysis will be presented in an upcoming paper (Germany *et al.* 1997).

We keep records of the limiting magnitudes resulting from each observation. The distribution for observations over the past year are shown in Figure 7. The median limiting search magnitudes are ~ 20.4 in R_M and ~ 20.5 in V_M , though we expect these limits to get fainter as we accumulate better templates. The large dispersion can be attributed to variation in sky conditions. A more complete discussion of our magnitude limits and their effects on the completeness of our search, as well as implications for the SN rate, will be presented in a paper currently in preparation (Reiss *et al.* 1997).

6. Determining the Motion of the Local Group

In this section we address how well we expect to be able to determine the motion of the Local Group (LG) relative to the Abell Clusters in our sample using SNe Ia. To do this, we have run a series of Monte Carlo simulations in which 10,000 fake samples have been created. The samples have varying sizes, geometries (in the sky), and bulk motion vectors. For the following discussion, all velocities mentioned are relative to the LG frame. In each case, the ‘fake’ supernovae have been given typical peculiar velocities of 400 km sec^{-1} (Marzke *et al.* 1995) on top of the flow velocity, distance uncertainties of 8%, and redshift uncertainties of 0.001 (in this redshift range, the overall errors are dominated by the distance uncertainties). The peculiar velocities which we are to use for our measurement are likely to be smaller ($\sim 250 \text{ km sec}^{-1}$) because we can use the average peculiar velocities of several galaxies in the host clusters for many of our SNe; however, note that we only include uncorrelated motions, and neglect small-scale correlated motions described in Watkins &

Feldman 1995, which Abell clusters are less sensitive to than galaxies in the field. Still, the uncertainties are dominated by the distance uncertainties (a distance uncertainty of 8% at $z=0.08$ is a $\sim 1900 \text{ km sec}^{-1}$ velocity uncertainty), so these simulations do not present unrealistic errors (this was verified by running simulations using different uncertainties and peculiar velocities). The redshift distribution of the SNe in the simulations mimics that of our cluster sample. Once the simulated SN sample is created, the best-fit values for the Local Group velocity vector, \vec{v}_{LG} , and the Hubble Constant, H_0 , for this sample are determined simultaneously by minimizing the statistic

$$\chi^2 = \sum_i \frac{(cz_i - H_0 d_i + \vec{v}_{LG} \cdot \hat{r}_i)^2}{\sigma_i^2}, \quad (3)$$

where d_i is the distance of the i th supernova, z_i is its redshift, \hat{r}_i is the unit vector pointing in its direction in the sky, and σ_i^2 is the quadrature sum of all errors mentioned above.

Of primary interest is estimating the accuracy with which our sample can be used to measure the reflex motion of the LG. To answer this, we compute the $1\text{-}\sigma$ dispersions in the 10,000 simulated dipole measurements for a sample geometry which matches that of our cluster targets. These are presented in Table 3 for the 3 velocity components, for a 20-, 40-, and 60-SN sample, using the parameters described above. The dispersions are identical for all sample geometries which we explored, and are independent of the direction of the input velocity vector. By blindly comparing these uncertainties to those quoted by LP in their 1994 measurement, $(\pm 250, \pm 273, \pm 198) \text{ km sec}^{-1}$, we find that applying ~ 35 SNe Ia distances collected in our sample to the problem results in a comparable measurement to that made using the 124 BCG distances of the LP sample. This is not surprising noting that SNe Ia are $\sim 2\times$ more accurate as distance indicators. For example, were we to make a velocity measurement, using the SNe Ia in our sample, that is consistent with the LP result, it would be significant at 2.3σ , 3.7σ , and 4.9σ levels for 20, 40 and 60 SNe Ia, respectively, compared to the COBE measurement. On the other hand, a measurement which coincides with the COBE dipole would rule out the LP result at the 1.9σ , 2.6σ , and 2.9σ levels (using the uncertainties of LP94). Note, however, that the simulated distance uncertainties of 8% are slightly greater than that estimated by Riess, Press, & Kirshner 1996 for their well-sampled SNe Ia light curves; this along with the high velocity dispersions used in the simulations, as pointed out above, implies that the results described here are probably slightly conservative. A comparison of the uncertainties listed in Table 3 for 20 SNe with those quoted by RPK95 (for 13 SNe) of $(\pm 370, \pm 510, \pm 220)$ confirms this notion.

In addition to estimating the expected uncertainties, the simulations also allow us to confirm that there will be a small geometric bias in any dipole measurement which is made using our sample, due to its non-uniform geometry (see Fig. 7). By comparing the

fits resulting from the simulated samples to their input dipole velocity vectors, we find that there will likely be a $\sim \pm 5 \text{ km sec}^{-1}$ offset in each vector component from the true value. The value will of course depend upon the actual geometry of the sample and the measured bulk motion, and can be easily computed and corrected, but it is still reassuring to find that it will be small compared to the expected uncertainties. We will investigate this, and other possible sources of systematic error, in a subsequent paper on the distance measurements from our first year's set of SNe.

We would like to thank the observatory director at MSSSO for his selection of this project for director's discretionary time. We are also grateful to M. Postman, T. Lauer, and M. Strauss for donating their compilation of cluster data for our target selection, and to A. Riess for his insightful comments on the manuscript. This research is supported by NSF grant AST 9617036 and by grants from the Seaver Institute and the Packard Foundation to the University of Washington.

REFERENCES

- Abell, G. O., Corwin, H. G., J., & Olowin, R. P. 1989, *Astrophys. J. Supp. Series*, 70, 1.
- Adams, M. T., Howell, D. A., Ward, M. H., Wheeler, J. C., & Wren, W. 1997, *IAU Circ #6674*.
- Branchini, E., Plionis, M., & Sciama, D. W. 1996, *Astrophys. J.*, 461, L17.
- Cappellaro, E., Turatto, M., Benetti, S., Tsvetkov, D. Y., Bartunov, O. S., & Makarova, I. N. 1993, *Astr. Astrophys.*, 268, 472.
- Ciardullo, R., Tamblyn, P., & Phillips, A. C. 1990, *Publ. Astr. Soc. Pacific*, 1113, 102.
- Colless, M. 1995, *Astron. J.*, 109, 1937.
- d. Li, W., l. Qiu, Y., y. Qiao, Q., Zhang, Y., Zhou, W., & y. Hu, J. 1997, *IAU Circ #6661*.
- Evans, C. R. & Kochanek, C. S. 1989, *Astrophys. J.*, 346, L13.
- Evans, R. 1997, *IAU Circ #6613*.
- Feldman, H. A. & Watkins, R. 1994, *Astrophys. J.*, 430, L17.
- Fixsen, D. J. *et al.* 1994, *Astrophys. J.*, 420, 445.
- Germany, L., Reiss, D., Schmidt, B. P., & Stubbs, C. W. 1997, *In Preparation*.
- Giovanelli, R., Haynes, M. P., Wegner, G., Da Costa, L. N., Freudling, W., & Salzer, J. J. 1996, *Astrophys. J.*, 464, L99.
- Graham, A. W. 1996, *Astrophys. J.*, 459, 27.
- Gramann, M., Bahcall, N. A., Cen, R., & Gott, J. R. 1995, *Astrophys. J.*, 441, 449.
- Groth, E. J. 1986, *Astron. J.*, 91, 1244.
- Hamuy, M. *et al.* 1995, *Astron. J.*, 109, 1.
- Hamuy, M. *et al.* 1996a, *Astron. J.*, 112, 2391.
- Hamuy, M. *et al.* 1996b, *Astron. J.*, 112, 2408.
- Hart, J. *et al.* 1996, *Publ. Astr. Soc. Pacific*, 108, 220.
- Hudson, M. J. & Ebeling, H. 1997, *Astrophys. J.*, 479, 621.

- Kim, A., Goobar, A., & Perlmutter, S. 1996, Publ. Astr. Soc. Pacific, 108, 190.
- Kolatt, T. S. & Bartelmann, M. 1997, MNRAS, *Submitted*.
- Lauer, T. R. & Postman, M. 1994, Astrophys. J., 425, 418. [LP94].
- Martin, R., Williams, A., & Woodings, S. 1997, *IAU Circ #6558*.
- Marzke, R. O., Geller, M. J., da Costa, L. N., & Huchra, J. P. 1995, Astron. J., 110, 447.
- Maza *et al.* 1997, *IAU Circ #6531*.
- Perlmutter, S. *et al.* 1997, Astrophys. J., 483, 595.
- Phillips, A. C. & Davis, L. E. 1995, in Astronomical Data Analysis Software and Systems IV, ed. R.A. Shaw, H.E. Payne, & J.J.E. Hayes, volume 77 of ASP Conference Series, 297.
- Phillips, M. M. 1993, Astrophys. J., 413, L105.
- Postman, M., Lauer, T. R., & Strauss, M. A. 1995, *Private Communication*. [PLS].
- Reiss, D., Germany, L., Schmidt, B. P., & Stubbs, C. W. 1997, *In Preparation*.
- Riess, A., Press, B., & Kirshner, R. P. 1995a, Astrophys. J., 438, L17.
- Riess, A., Press, B., & Kirshner, R. P. 1995b, Astrophys. J., 445, L91. [RPK95].
- Riess, A., Press, B., & Kirshner, R. P. 1996, Astrophys. J., 473, 88.
- Riess, A. G., Davis, M., Baker, J., & Kirshner, R. P. 1997, ApJ, *Submitted*.
- Schechter, P. L., Mateo, M., & Saha, A. 1993, Publ. Astr. Soc. Pacific, 105, 1342.
- Schmidt, B. P. *et al.* 1997a, ApJ, *Submitted*.
- Schmidt, B. P. *et al.* 1997b, Bull. American Astron. Soc., 189(108).
- Strauss, M. A., Cen, R., Ostriker, J. P., Lauer, T. R., & Postman, M. 1995, Astrophys. J., 444, 507.
- Stubbs, C. W. *et al.* 1993, in Proceedings of the SPIE, volume 192, 1900.
- Tammann, G. A. 1994, in "Supernovae", Les Houches 1990, Session LIV, ed. S. A. Bludman, R. Mochkovitch, & J. Zinn-Justin,), 3.

- Treffers, R. R., Peng, C. Y., Filippenko, A. V., & Richmond, M. W. 1997, *IAU Circ #6627*.
- Watkins, R. & Feldman, H. A. 1995, *Astrophys. J.*, 453, L73.

7. Figure Captions

Fig. 1.— The distribution of target clusters in the sky, in galactic (top) and equatorial (bottom) coordinates. Filled square symbols represent clusters whose BCG distances were measured by LP94, filled circles were not. Thin circles enclose those clusters in which this project has found a supernova since June 1996 (several have two SNe). Also shown are the direction of the LP94 bulk flow (LP), and the direction of the Fixsen *et al.* 1994 microwave background dipole (CMB).

Fig. 2.— The distribution in seeing FWHM on the 1.3m telescope at Mt. Stromlo over a year. Median seeing is $\sim 2.5''$.

Fig. 3.— A histogram of the number of days between each cluster observation (Δt). Top: The observations of June 1996 to the present; Bottom: A simulation of observations over a 3-year period.

Fig. 4.— The search process illustrated on a subsection of the images in which SN 1996aj in Abell 3559 was detected. Fig. (a) shows a template, with a grid of 9 false sensitivity stars and masked saturated regions. The observation (b) is registered to the template (c). Fig. (d) shows the template of Fig. (a) after it has been convolved so that its PSF matches that of the registered image (c). After the registered image has been flux-matched to the convolved template, the template is subtracted. The residual is shown in Fig. (e), with the supernova (center) and five sensitivity stars clearly visible.

Fig. 5.— A subraster of an SN candidate, produced by the search software. This is the actual subraster created for SN 1996aj seen in Fig. 7e. The supernova is clearly visible in both colors (SN), as are two cosmic rays (CRs, convolved during the subtraction process) in the V observation and subtraction.

Fig. 6.— Distribution of limiting magnitudes for all observations for which this was measurable. Typical median limits have been ~ 20.4 in R_M and ~ 20.5 in V_M .

TABLE 1. List of target clusters in the Mount Stromlo Abell Cluster Supernova Search.

Abell	α	J2000	δ	N_{gal}
119	00 56.35		-01 15.78	69
151	01 08.87		-15 25.02	72
168	01 15.16		+00 13.85	89
279	01 56.37		+01 03.65	70
401	02 58.95		+13 34.93	90
423	03 11.29		-12 06.72	89
514	04 47.67		-20 26.73	78
5481	05 45.17		-25 52.00	80
5482	05 48.67		-25 27.00	80
754	09 08.83		-09 39.20	92
1020	10 27.84		+10 24.67	68
1066	10 39.40		+05 10.35	68
1317	11 35.13		-13 31.60	82
1644	12 57.24		-17 22.22	92
1648	12 59.00		-26 38.18	68
1736	13 26.87		-27 07.55	104
1773	13 42.14		+02 14.88	66
1780	13 44.64		+02 52.97	71
1809	13 53.31		+05 10.25	78
2029	15 10.98		+05 45.70	82
2362	21 40.73		-14 16.35	69
2401	21 58.87		-20 06.63	66
2480	22 46.08		-17 41.18	108
2559	23 13.12		-13 41.67	73
2661	23 46.67		-10 25.33	147
2670	23 54.17		-10 24.30	142
2819	00 45.82		-63 35.62	90
2889	01 14.76		-48 30.15	65
2954	01 54.47		-71 28.32	121
2995	02 15.18		-24 50.07	69
3094	03 11.44		-26 55.73	80
3108	03 15.24		-47 37.95	73
3112	03 17.94		-44 14.10	116
3122	03 22.30		-41 20.33	100
3128	03 30.21		-52 33.80	140
3135	03 34.04		-39 00.02	111
3142	03 36.71		-39 48.17	78
3158	03 43.01		-53 38.57	85
3188	03 57.77		-27 02.45	67
3202	04 00.25		-53 39.62	65
3223	04 08.57		-30 49.13	100
3231	04 11.87		-64 36.40	65
3266	04 31.16		-61 28.67	91
3301	05 00.80		-38 40.67	172
3341	05 25.59		-31 35.43	87
3381	06 09.92		-33 35.65	69
3392	06 27.07		-35 28.90	77
3490	11 45.31		-34 26.67	91
3528	12 54.30		-29 01.27	70
3549	13 14.36		-29 26.87	65
3558	13 27.91		-31 29.53	226
3559	13 29.90		-29 31.47	141

TABLE 1. (continued)

Abell	α	J2000	δ	N_{gal}
3560	13 31.84		-33 13.42	184
3562	13 33.53		-31 40.37	129
3566	13 38.99		-35 33.22	100
3571	13 47.48		-32 51.95	126
3577	13 54.34		-27 50.72	103
3651	19 52.18		-55 05.27	75
3667	20 12.50		-56 49.00	85
3698	20 35.98		-25 16.57	71
3716	20 51.55		-52 42.73	66
3744	21 07.23		-25 28.90	70
3775	21 31.60		-43 18.75	76
3781	21 34.63		-66 50.63	79
3806	21 46.63		-57 17.12	115
3809	21 46.96		-43 54.10	73
3822	21 54.10		-57 50.82	113
3825	21 58.37		-60 23.67	77
3831	22 03.33		-45 49.47	81
3879	22 27.83		-69 01.68	114
3990	23 18.77		-67 46.58	98
4008	23 30.29		-39 19.45	66
4038	23 47.70		-28 08.33	117
4059	23 56.68		-34 40.30	66